How to cite: *Angew. Chem. Int. Ed.* **2025**, *64*, e202411772
doi.org/10.1002/anie.202411772

Polymer Chemistry

Thermally Assisted Microfluidics to Produce Chemically Equivalent Microgels with Tunable Network Morphologies

Dirk Rommel, Bernhard Häßel,* Philip Pietryszek, Matthias Mork, Oliver Jung, Meike Emondts, Nikita Norkin, Iris Christine Doolaar, Yonca Kittel, Ghazaleh Yazdani, Abdolrahman Omidinia-Anarkoli, Sjören Schweizerhof, Kyoohyun Kim, Ahmed Mourran, Martin Möller, Jochen Guck, and Laura De Laporte**

Abstract: Although micron-sized microgels have become important building blocks in regenerative materials, offering decisive interactions with living matter, their chemical composition mostly significantly varies when their network morphology is tuned. Since cell behavior is simultaneously affected by the physical, chemical, and structural properties of the gel network, microgels with variable morphology but chemical equivalence are of interest. This work describes a new method to produce thermoresponsive microgels with defined mechanical properties, surface morphologies, and volume phase transition temperatures. A wide variety of microgels is synthesized by crosslinking monomers or star polymers at different temperatures using thermally assisted microfluidics. The diversification of microgels with different network structures and morphologies but of chemical equivalence offers a new platform of microgel building blocks with the ability to undergo phase transition at physiological temperatures. The method holds high potential to create soft and dynamic materials while maintaining the chemical composition for a wide variety of applications in biomedicine.

Introduction

Microgels have an increasingly growing array of applications in biomaterial, medical as well as process engineering fields that often overlap in their interdisciplinary research due to the generally relevant challenges. Micron-scale microgels in particular have gained a lot of interest as injectable building blocks to create soft three-dimensional regenerative materials with unique properties like micro- to macroporosity and alignment.[1] Here, microfluidic techniques,[2] stop-flow lithography,[3] and in mold polymerization[4] have been extensively developed and implemented to produce microgels with different physical and mechanical properties. It is important to point out that this paper focuses on micron-scale microgels which can later be used to support and influence cell growth. They are not meant to be injected in the blood stream, nor should they be taken up by cells. One of the remaining key challenges of these types of microgels is the structural fine-tuning of the microgel network to control their functionality and responsivity. While the level of stiffness, diffusion properties, and (bio)chemical modification were extensively studied,[5] varying the gel network

[*] Dr. D. Rommel, B. Häßel, P. Pietryszek, M. Mork, O. Jung, Dr. M. Emondts, N. Norkin, I. C. Doolaar, Y. Kittel, G. Yazdani, Dr.-Ing. A. Omidinia-Anarkoli, Dr. A. Mourran, Prof. M. Möller, Prof. L. De Laporte
DWI—Leibniz Institute for Interactive Materials e. V.
Forckenbeckstrasse 50, 52074 Aachen, Germany
E-mail: delaporte@dwi.rwth-aachen.de

Dr. D. Rommel, B. Häßel, P. Pietryszek, M. Mork, O. Jung, I. C. Doolaar, Y. Kittel, Dr. S. Schweizerhof, Prof. M. Möller, Prof. L. De Laporte
Institute for Technical and Macromolecular Chemistry
RWTH Aachen University
Worringerweg 1–2, 52074 Aachen, Germany

N. Norkin
Institute of Bioengineering, School of Life Sciences,
École Polytechnique Fédérale de Lausanne (EPFL)
Lausanne, Switzerland

N. Norkin
Institute of Mechanical Engineering,
École Polytechnique Fédérale de Lausanne (EPFL)
Lausanne, Switzerland

Dr. K. Kim, Prof. J. Guck
Max Planck Institute for the Science of Light
and
Max-Planck-Zentrum für Physik und Medizin
Staudtstraße 2, 91058 Erlangen, Germany

Prof. J. Guck
Department of Biophysics and Bioinformatics
BIOTEC—Biotechnology Center
Dresden University of Technology
Tatzberg 47/49, 01307 Dresden, Germany

Prof. L. De Laporte
Department of Advanced Materials for Biomedicine (AMB)
CBMS—Center for Biohybrid Medical Systems
AME—Institute of Applied Medical Engineering
RWTH Aachen University
Forckenbeckstraße 55, 52074, Aachen, Germany
E-mail: delaporte@dwi.rwth-aachen.de

architecture on the molecular and macromolecular scale is still a poorly explored field of work.

In good solvents, step-growth polymerization and crosslinking tend to result in more homogeneous gel networks with more defined pore sizes, while chain-growth mechanisms like free-radical polymerization (FRP) are known to form more heterogeneous networks.[6] Chain-growth network architectures include features such as loose polymer chains or loops caused by intramolecular chain transfer, which do not contribute to the stability of the network. They have a more heterogeneous spatial material distribution with statistically higher and lower densities of crosslinked polymer clusters. As the molecular weight drastically increases during crosslinking, the soluble monomers and oligomers become immobilized as part of the gel network. In one recent work, reported by our group, we demonstrated how FRP of different polymer architectures, molar masses, and concentrations alter the polymer network of poly (ethylene glycol)-based rod-shaped microgels and its related mechanical properties, degree of swelling, mesh size, diffusion properties, and free reactive groups for post-functionalization of the microgels.[7] In some cases, these polymer networks can undergo a change in interaction with the surrounding solvent.[6,8] A prominent application of this process is precipitation polymerization, mainly leading to microgels with submicron diameters.[9]

Thermoresponsive *N*-isopropylacrylamide (NIPAm)-based homopolymers with their characteristic lower critical solution temperature (LCST) of ~32 °C in water, along with their copolymers are studied extensively[9a,10] due to their promising potential for various material science applications.[10b,11] *N*-ethylacrylamide (NEAm) is a chemically very similar monomer to NIPAm differing in the absence of one methyl group, resulting in homopolymers with a LSCT of ~73 °C in water.[12] It was shown that the random copolymerization of NIPAm and NEAm allows for altering the resulting volume phase transition temperature (VPTT) of the gel network based on the NIPAm/NEAm ratio.[13] In addition, the architecture of the network can also be varied by using the cononsolvency effect of the thermoresponsive polymers.[13b,14]

The thermoresponsiveness of PNIPAm-based gels has been employed to mechanically influence living cells, showing effects on mechanosensitive proteins and affecting their proliferation.[15] By embedded gold nanorods (AuNR) inside the gel that are able to convert pulsating near infrared (NIR) light into rapid heating-cooling cycles, PNIPAm-based gels can be used as platforms for photothermal actuation.[16] We previously reported the applicability of patterned statistical P(NIPAm-*co*-NEAm) hydrogels with AuNR to actuate cells up to 10 Hz at physiological temperatures for several days.[13c,17a,b] In these three studies, no signs of cell toxicity were observed. When modified with cell adhesive proteins, cells adhered, spread, and grew well on top of these hydrogels. The actuating hydrogel system was used as in vitro *gym* to trigger mechanosensitive pathways inside the cells, influencing their interaction with the substrate, their shape and dimensions, cell migration, nuclear shuttling of mechanosensitve proteins, the production of extracellular matrix proteins, and proliferation and differentiation of cells via photothermal volume actuation. The suitable comonomer molar ratio of NIPAm to NEAm (1.5) was determined to set the hydrogel's VPTT to ~37 °C in cell culture medium, and the optimal monomer weight percentage (57 w/v% with 1.4 wt% crosslinker) was defined to achieve sufficient actuation amplitudes, while supporting cell adhesion via a covalently linked fibronectin or collagen coating. The relative shallow slope of the volume phase transition, however, limits the actuation amplitude in the narrow cell-relevant temperature range of 36–39 °C, while the smooth hydrogel surface does not have a nano-topography that is known to further influence cell interaction and force transmission.[18] To increase the range of responsiveness, mechanical properties, and surface topography of the thermoresponsive P(NIPAm-*co*-NEAm) gel networks and transfer this in vitro gym concept from a 2D patterned hydrogel film to 3D microgels, comonomers or star-shaped P(NIPAm-*co*-NEAm)-based precursor molecules are synthesized and crosslinked using thermally assisted droplet-based microfluidics. While maintaining the similarity of the chemical components, a wide platform of microgels with different internal macromolecular and morphological structures are produced, affecting their thermoresponsivity. This way, the gel properties, such as stiffness or roughness, can be adjusted at the molecular and macroscopic level while simultaneously tuning the extent of thermoresponsive volume change.

To obtain this library of micron-scale thermoresponsive microgels, three different types of precursor solutions are used and microfluidic microgel production is performed at temperatures below and above the LCST of the copolymer. All gel precursor systems consist of a preset equal ratio of NIPAm and NEAm. To achieve differing internal structures in microgels, star-shaped polymers with a low dispersity ($Đ \approx 1.21$) are synthesized via reversible addition-fragmentation chain transfer polymerization (RAFT) using self-synthesized chain transfer agents (CTAs). These thermoresponsive multi-arm molecules are further functionalized with methacrylate end groups to obtain rapidly crosslinkable stars via FRP.

To investigate the effect of the precursor composition, hydrogels and microgels from 3- and 4-armed star polymers, as well as a combination of NIPAm, NEAm and *N*,*N*′-methylenebisacrylamide (MBA) are produced using a defined set of operational parameters (flow rates, chip design, continuous phase) in the specially developed, thermally assisted microfluidics setup. Depending on the precursor molecular architecture, in combination with the controlled reaction conditions during gelation, the internal structure of the gel network is altered, determining the functional properties of the microgels. The combination of dynamic crosslinking and temperature-dependent dewetting processes during gelation in thermally assisted microfluidics results in microgels with significantly differing morphologies and responsivities.

Results and Discussion

Thermally Assisted Microfluidics Design

To obtain a library of micron-scale thermoresponsive microgels with different mechanical properties, surface topographies, and responsivity under physiological conditions, different precursors are synthesized and crosslinked with thermally assisted microfluidics below and above the transition temperature. As the formation of a covalent microgel network is a highly complex process determined by factors, such as precursor diffusion, polymer solubility, and the chemical reaction kinetics, the temperature greatly influences the dynamic shift during this gelation process. 3- and 4-armed star polymers with a thermoresponsive P(NIPAm-*co*-NEAm) chain and reactive methacrylate (MA) end groups are synthesized by reversible addition – fragmentation chain-transfer (RAFT) polymerization and successive end-group transformation. These star polymers are employed to produce microgels in a novel thermally assisted microfluidic method and compared with the same molar ratio of NIPAm and NEAm monomers in combination with MBA as crosslinker. The effect of temperature during crosslinking on the microgel properties is studied.

To obtain chemically equivalent compositions in the different precursor solutions, tri- and tetrafunctional trithiocarbonate CTAs are synthesized and utilized for statistical RAFT-copolymerization of NIPAm and NEAm of an equal molar ratio of 1.5, resulting in the 3- and 4-arm copolymers (Scheme S1a–b). The trithiocarbonyl end groups (TTC) are converted into MA end groups via a phosphine-catalyzed aminolysis reaction (Scheme S1c).

The three precursor systems consist of LAP as photoinitiator and either the NIPAm and NEAm monomers plus MBA crosslinker (MC), the 3S components, or 4S-componens (Scheme 1a–c). Rhodamine-B methacrylate acts as covalently incorporated fluorescent marker within the aqueous phase. The flow rates of the continuous oil phase in combination with the aqueous dispersed precursor phases allow for setting the precursor droplets to the same size. The additional second oil inlet controls the overall flow rate from the microfluidic chip into the polyethylene (PE) tube compensating for the deviations between the flow rates due to differences in rheological properties of the respective precursor systems (Scheme 1c, Table S1). This prevents superposition and accumulation of dispersed droplets during UV-irradiation.

The thermally assisted microfluidic setup used for this study includes sufficient length of the PE tube to achieve a constant controlled temperature during gelation (Supporting Information: Heat transfer during thermally assisted microfluidics). The irradiation time and intensity are defined by the custom-built UV lamp ($\lambda = 365$ nm, 30.36 mW cm^{-2}, Table S1). The product is collected and purified by applying washing cycles consisting of supernatant removal after sedimentation and redispersion in fresh solvent (Scheme S5c).

Precursor Synthesis and Gelation

The reactive 3- and 4-arm copolymers are synthesized from statistical RAFT-copolymerization of NIPAm and NEAm of an equal molar ratio of 1.5. The obtained precursor molecules are characterized by nuclear magnetic resonance spectroscopy (NMR) (NMR data available in Supporting Information) and gel permeation chromatography (GPC) (Figure 1a). For the 3- and 4-armed methacrylate-terminated precursor molecules (3-NNMA and 4-NNMA), the weight average molecular weight *Mw* calculated per arm differs by ~217 g mol^{-1} (Figure 1a), which is approximately the sum of one NIPAm and NEAm monomer each (212 g mol^{-1}). However, the GPC only serves to estimate the relative mass distribution of the products as no specific star-shaped calibration standards are available for this novel polymer system and linear poly(methyl methacrylate) standards are employed here.

To compare the gelation kinetics and hydrogel properties obtained from crosslinking the three different precursor solutions (MC, 3S, 4S as aqueous solutions $c = 25$ wt%), bulk hydrogels are prepared at room temperature and analyzed with rheology. The most rapid gelation and highest stiffness is observed for MC, likely due to superior diffusion kinetics of the monomer-based species during gelation along with the statistically less favored intra-chain cyclization compared to the star-based precursors (Figure 1b).[19] The obtained gelation times are used to adjust the flow rates for thermally assisted microfluidics towards complete gelation (Figure 1b, Table S1). The higher stiffness of 4S in comparison to 3S (Figure 1c) could be associated with the thicker polymer walls (Figure 1d), which could arise from more pronounced intermolecular interaction during the gelation process leading to more spatially compacted regions. At the same time, 4S leads to a significantly higher loss modulus compared to 3S (Figure 1c). Respective tanδ values (Table S3) indicate presumably different deformabilities between the gel networks based on the corresponding precursor system.

Gelation Temperature Affects Microgel Internal Structures

The synthesis with different precursor architectures allows for rapid gelation yet results in significantly distinguishable hydrogel properties. In the following, gelation of the three precursor systems is performed using thermally assisted microfluidics to continuously fabricate microgels while varying the gelation parameters by changing the temperature during UV-triggered crosslinking. Depending on the precursor system and gelation temperature (GT) ranging stepwise from 23 to 55 °C, the microgel polymeric network structures differ. The images of the microgel spheres taken at room temperature show an increase in light scattering, i.e. darker appearance, indicating an increase in phase separation during gelation above the LCST of the polymers (Figure 2a). To provide a three-dimensional analysis of the obtained microgel morphologies, confocal laser scanning microscopy (CLSM) is employed (Figure 2b–c).

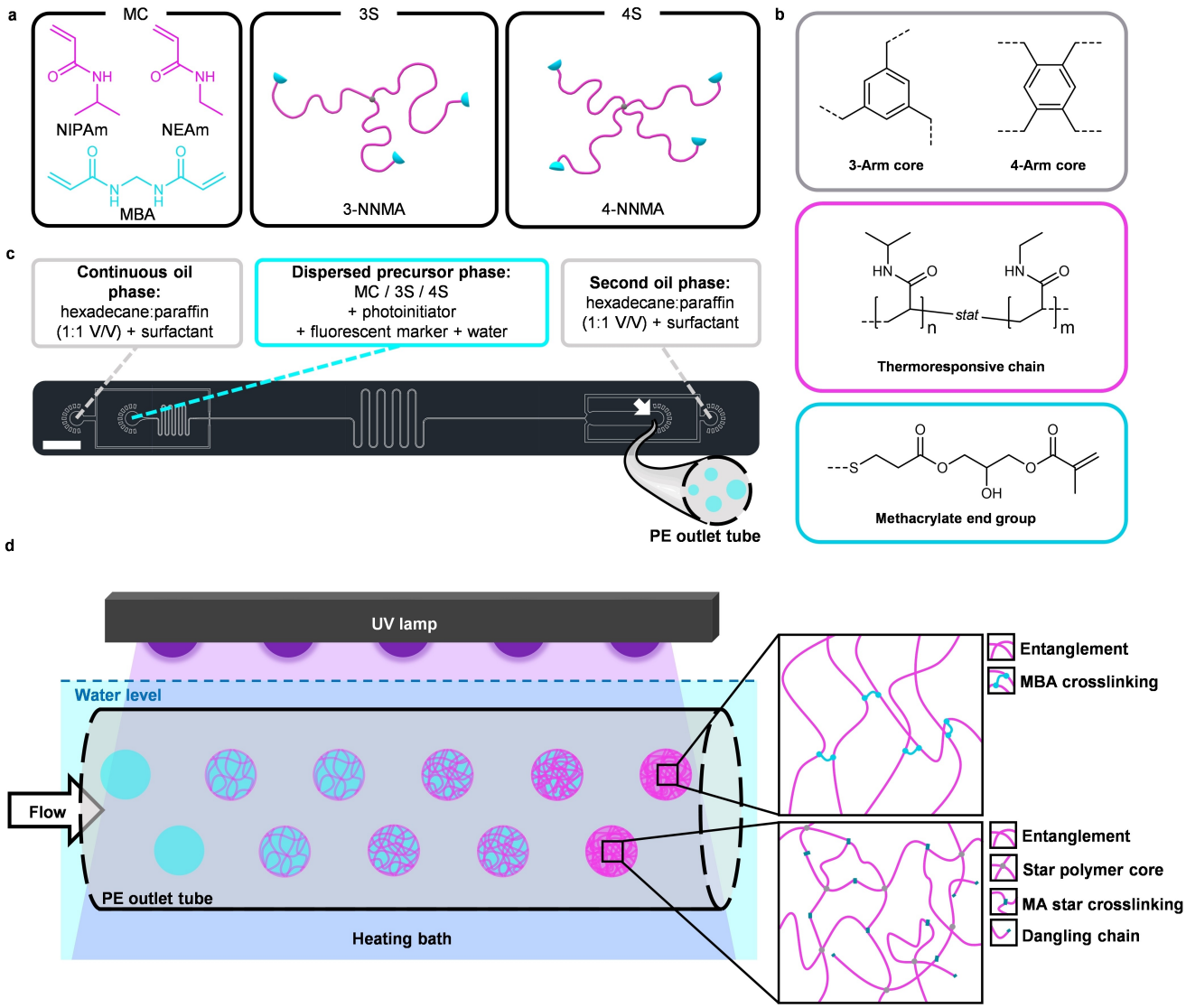

Scheme 1. Combination of the different precursor systems and thermally assisted microfluidics setup. a) Chemical structures NIPAm, NEAm and MBA molecules comprising the monomer plus crosslinker (MC) system and schematic representation of 3S and 4S precursor systems. b) Chemical composition of 3- and 4-NNMA molecules. c) Compositions of the dispersed and the continuous phases used in thermally assisted microfluidics and their corresponding inlet position at the microfluidic chip design. The white arrow indicates the position of the outlet and the transition to the outlet polyethylene (PE) tube. Scale bar represents 2 mm. Detailed dimensions of the chip design can be found in Supporting Information Scheme S2. d) The outlet PE tube containing the droplets filled with the dispersed precursor solution is placed in a tube in a water bath with controlled temperature where it is exposed to a UV-lamp to initiate free-radical induced gelation. Inserts show simplified network structure of microgels derived from MC (top) and 4S (bottom). Corresponding chemical structures are depicted in Supporting Information Scheme S3 and S4. More details about the irradiation setup can be found in the Supporting Information Scheme S5a–b and S6.

Thermally assisted microfluidics enables the continuous fabrication of microgels, which undergo a thermally related morphology change during the gelation event. The phase separation process inside the droplets effects formation of droplets that form a void in the polymer network due to the depletion of reactive components. This state is chemically frozen after gelation and the further it has developed, the larger the voids become. The MC system shows a more gradual transition between 30 and 35 °C GT, which is associated with the LCST of PNIPAm-homopolymer in water (~32 °C). Once oligomers consisting of PNIPAm reach a significant polymerization degree, phase transition takes place and influences further formation of the gel network. With increasing temperature, the polymer LCST is reached for a greater number of growing macromolecules, as the presence of PNEAm increases the transition temperature required to induce phase transition. For the star-based 3S and 4S microgels, a clear morphology transition can be observed between 40 and 45 °C (Figure 2a), which is associated with the already preprogrammed LCST at ~45 °C in water set by the NIPAm to NEAm ratio (1.5) during the RAFT copolymerization (Scheme S1a–b). Assuming that a

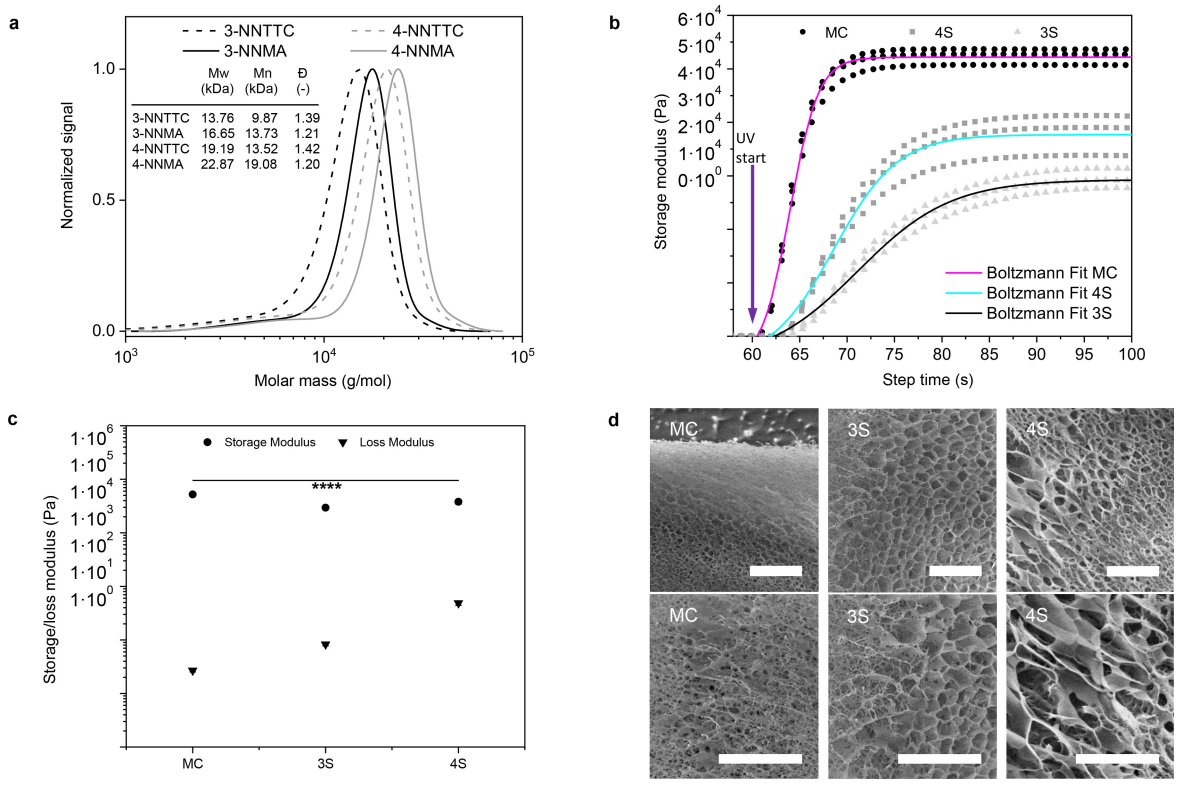

Figure 1. Precursor and hydrogel properties. a) Molecular weight distributions of TTC- and MA-terminated star polymers obtained via GPC. b) Precursor dependent gelation kinetics obtained via UV-assisted rheometry. Continuous UV-irradiation starts after 60 s of equilibration time. Individual data points ($n=3$ for each precursor system) are used for the respective combined fit starting from the irradiation. c) Storage and loss moduli of the three different precursor solutions after gelation at room temperature measured by shear rheometry. Error bars represent ± SEM, *P*-values are calculated using one-way ANOVA with Bonferroni correction, ****$P<0.0001$, $n=3$. d) Cryo-field emission scanning electron microscopy (cryo-FESEM) images of hydrogels from the three respective precursor solutions. Scale bars represent 5 µm.

similar amount of the precursor material was incorporated in all microgels (precursor $c=25$ wt% and reaction parameters set towards complete conversion), the observed refraction occurs due to the characteristic network structure formed.

All gels prepared from the three precursor systems show a homogeneous fluorescent signal distribution when prepared at GT: 23 °C (Figure 2b). However, at GT: 55 °C, the same precursor systems result in completely different morphologies (Figure 2c). At GT: 55 °C, the MC precursor forms microgels consisting of locally compacted interlinked porous material. The resulting pores are interconnected and thus form an open structure. Microgels produced from 3S at GT: 55 °C show separated pores in the micron-scale indicating dewetting processes at a larger scale. The microgels' surface of 3S is smooth while MC microgels have an irregularly grainy shaped surface (Figure 2c). The most significant dewetting is observed for the microgels produced with 4S at GT: 55 °C. This composition results in hollow microgel spheres, which are created by precursor migration and accumulation from the aqueous phase towards the outer oil phase during gelation, forming a smooth edge toward the microgel core with semicircular dents on the surface. These dents are assumed to result from water displacement out of the dense hydrophobic polymer network being crosslinked. While most of the water of the dispersed inner precursor droplet is located at the core during gel network formation, which contributes to the hydrophobic precursor material being uniformly distributed forming the smooth inner edge, residual water is trapped between the hydrophobic polymer network and the outer continuous oil phase. The observed shape indicates the presence of these trapped residual water droplets during the gelation event. Although both star-based precursor systems form closed networks lacking interconnected micropores, the dewetting processes differ drastically, resulting in individual morphologies. Videos of z-stack scans of the microgels (Figure 2b–c) are provided in the Supporting Information (Movie S1). To classify the properties of the obtained microgels, further mechanical and temperature-assisted analytical techniques are implemented to compare stiffness and temperature-induced transitions.

Microgel Mechanical Properties and Thermoresponsive Behavior

The effective Young's moduli of the microgels are measured with nanoindentation, revealing significant changes for the different precursor systems and correlating with the gelation temperatures (Figure 3a). The stiffest microgels are prepared using the 3S system at GT: 55 °C resulting in a mean

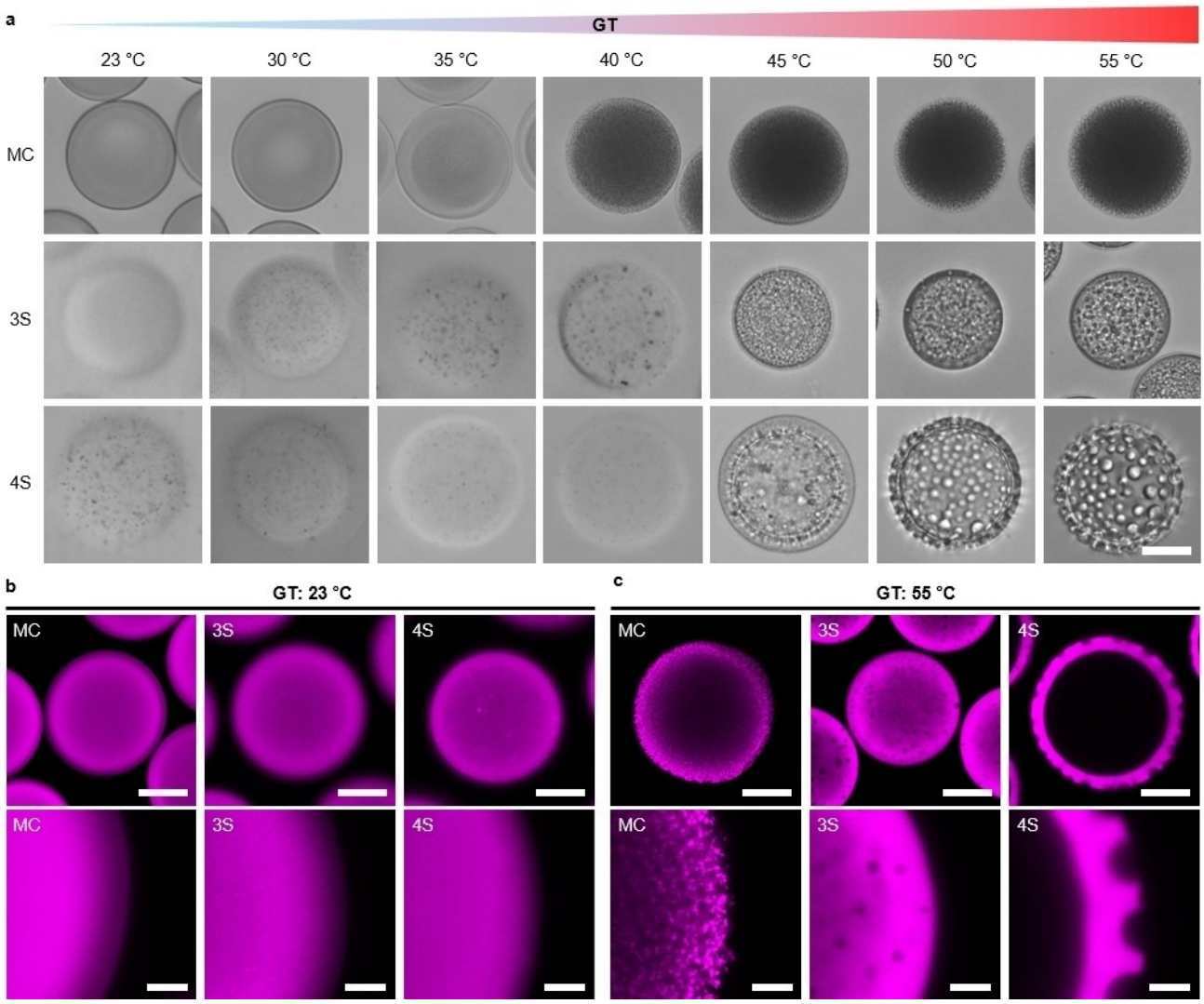

Figure 2. Bright-field and confocal laser scanning microscopy of spherical microgels produced at different gelation temperatures (GT). The fluorescent signal deriving from covalently bound rhodamine B allows for a qualitative comparison of the resulting gel network structures. a) Bright-field images of microgels fabricated at seven different gelation temperatures (23, 30, 35, 40, 45, 50 and 55 °C). Bright-field images taken after purification at room temperature in water after equilibration time of 10 min. Scale bar represents 50 µm. b) Microgels produced at GT: 23 °C showing a homogeneous morphology. c) Microgels produced at GT: 55 °C showing phase separation and precursor type-specific heterogeneous morphologies. Scale bars represent 50 µm for the upper and 10 µm for the lower images. Confocal images are taken as z-stacks at the middle height of each microgel after purification at 23 °C.

effective Young's modulus of 173.8 ± 37.8 kPa, while GT: 23 °C leads to the overall softest microgels with values of 1.0 ± 0.4 kPa. While increasing GT results in increasing effective Young's moduli for both the star-based systems, the values measured for the MC system decrease accordingly. The weaker connection points in between the locally compacted networks, in combination with the interconnected porous morphology (Figure 2c: MC GT: 55 °C), likely allows for deformation of the microgel compensating the mechanical stress applied by the probe and thus resulting in lower values. The longitudinal moduli of microgels formed at GT: 23 °C are measured by Brillouin microscopy (Figure 3b). The microgels produced at GT: 55 °C are not sufficiently transparent to apply this method. Results agree with those obtained from nanoindentation, which is consistent with previously reported empirical correlations between the longitudinal modulus and Young's modulus for biological samples.[7,20] The mass density of microgels measured by optical diffraction tomography (ODT) also follows the same trend measured by nanoindentation and Brillouin microscopy (Figure 3c). This correlation may suggest that the increased mass density in microgels can strengthen the mechanical stiffness within the networks.[21] Interestingly, even though the differences in Young's modulus between the microgels made from the 3S and 4S system are similar at GT: 23 °C, both the longitudinal modulus and mass density are higher for the 4S microgels.

The microgel diameters are quantified during active heating-cooling cycles. Microgel diameters for all GT parameters are measured in water at 23 and 55 °C after an

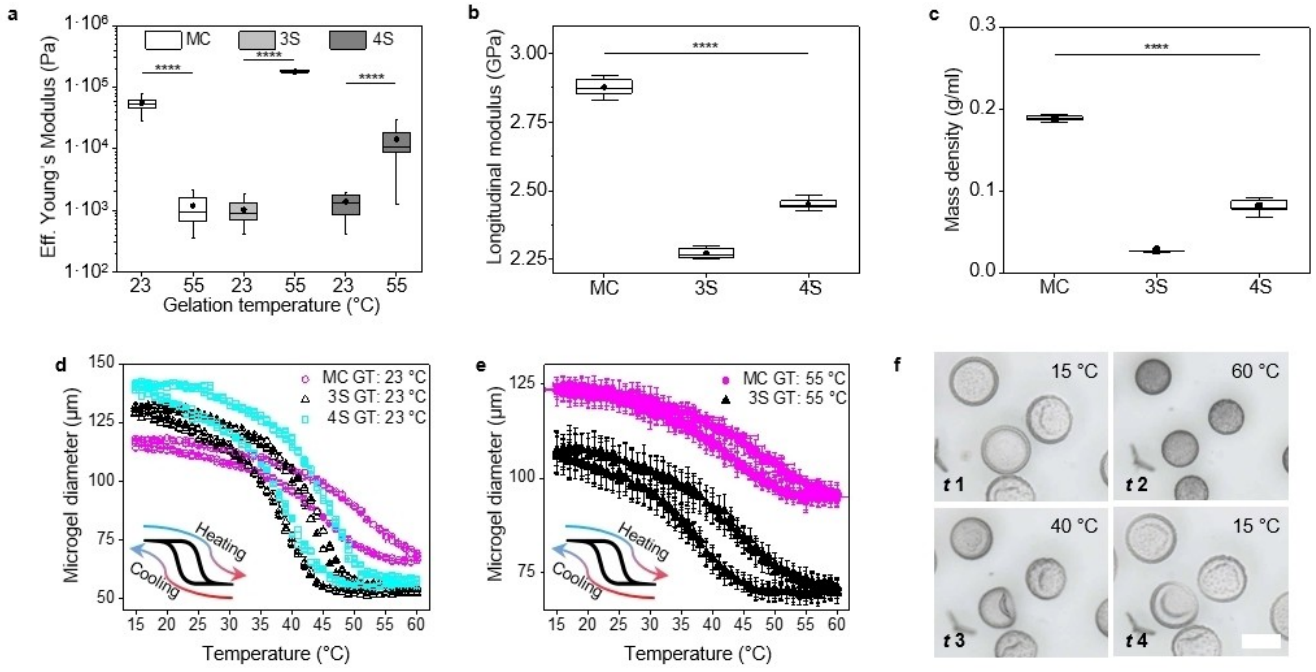

Figure 3. Mechanical properties quantification. a) Effective Young's moduli of selected microgels measured via nanoindentation ($n \geq 14$). b) Longitudinal moduli determined via Brillouin frequencies of microgels prepared at GT: 23 °C ($n = 10$). c) Mass densities calculated from refractive indices measured via ODT of microgels prepared at GT: 23 °C ($n = 10$). Error bars represent ± SEM, *P*-values are calculated using one-way ANOVA with Bonferroni correction, $*P < 0.05$, $***P < 0.001$, $****P < 0.0001$. Data displayed as a box plots, extending from the 25th to 75th percentile and the whiskers reaching from 5 % to 95 % quantiles. The lines represent the medians and black points indicate means. d–e) Dimensions measured during heating-cooling cycles ($\Delta T = 15$ °C/min) of MC, 3S and 4S microgels prepared at GT: 23 °C (d), and of MC and 3S microgels prepared at GT: 55 °C (e). Data displayed as means and error bars represent ± SEM ($n = 3$). f) Bright-field images displaying the heating-cooling cycles for the 4S GT: 55 °C microgels. Heating leads to isometric microgel collapse (*t* 1–*t* 2). Cooling results in anisometric microgel deformation (*t* 2 –*t* 4). Scale bars represent 100 µm.

equilibration time of 10 min (Figure S1). For all microgels, the ratio between the swollen (23 °C) and collapsed (55 °C) state decreases with increasing GT, likely due to the higher rigidity of the denser polymer walls between the pores due to phase separation-initiated local compaction of material, resulting in less deformability of the obtained gel network. Next, constant heating-cooling rates ($\Delta T = 15\,°C\,min^{-1}$) are employed for the microgels produced at GT: 23 and 55 °C, resulting in hysteresis curves (Figure 4d–e). In the case of slower heating-cooling rates ($\Delta T = 5\,°C\,min^{-1}$), only a small hysteresis is observed (Figure S2), while for higher heating-cooling rates, higher hysteresis occurs and low-resolution data is achieved. For the GT: 23 °C microgels, the total diameter changes throughout the heating-cooling cycle

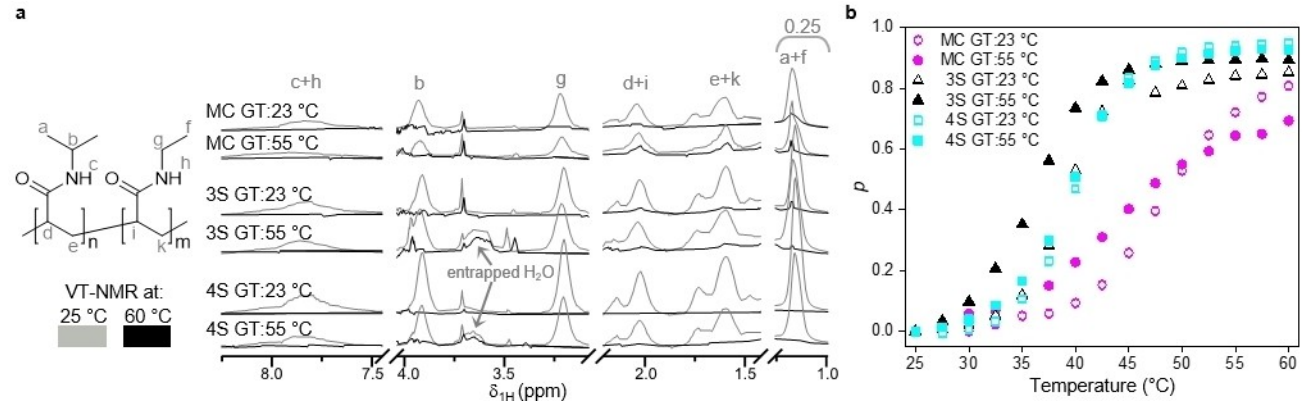

Figure 4. Temperature-dependent NMR analysis of microgels. a) ^{1}H HR-MAS NMR spectra (700 MHz, H_2O/D_2O, 4 kHz spinning frequency) at 25 °C (grey) and 60 °C (black) of MC, 3S and 4S microgels prepared at GT: 23 °C and GT: 55 °C. The intensities of the signals a + f are adjusted by a factor of 0.25, respectively. b) Variable temperature NMR to determine the phase separated fraction of the CH_3 sidegroups *p* (a + f).

correlates well with the microgel diameters measured at 23 and 55 °C (Figure S1). The higher deformability of 4S compared to 3S microgels prepared at GT: 23 °C might be explained by the higher tanδ values measured for the 4S-based hydrogel networks via rheometry (Table S3) in combination with its network morphology (Figure 1d). These microgels start from a more swollen state compared to the 3S microgels. The GT: 55 °C microgels exhibit an overall lower extent of volume transition between the swollen and collapsed state compared to their GT: 23 °C counterparts (Figure 3d–e). The least pronounced hysteresis is observed for the MC GT: 55 °C microgels. This suggests that water transport during the heating-cooling cycles is less hindered for the interconnected porous gel network of MC GT: 55 °C microgels (Figure 2c), in comparison to all other samples where variable water diffusion out of the network during heating (collapsing) and into of the network during cooling (swelling) affect the dynamics of the microgel volume change. The most significant effect of the microgels' water permeability is visible in the shape deformation hysteresis of the hollow 4S GT: 55 °C microgels, as it is amplified by its hollow shape. While an isotropic shrinkage is observed during heating, the shells undergo an inwards buckling deformation during the cooling phase (Figure 3f: *t* 2–*t* 4). Assuming that there is no spatial temperature gradient across the shell, the swelling process, i.e. water uptake, during cooling happens symmetrically. Therefore, the shell grows isotropically, whereas the inner volume is insufficiently supplied with water during this process due to the hindered diffusion of water from the environment through the gel network of the shell. As the shell grows faster than its inner volume, the geometric incompatibility induces an inwards buckling deformation, enabled by the flexible nature of the gel. Subsequent heating of the hollow microgels allows for reversible deformation back to the spherical geometry (Figure 3f: *t* 2, Movie S2).

To investigate the thermoresponsive behavior of the microgels, their temperature-dependent accessible chemical composition on a molecular level is analyzed by magic-angle spinning (MAS) ^{1}H NMR spectroscopy. Figure 4a shows selected regions of ^{1}H NMR spectra before and after microgel volume phase transition, and the corresponding assignments of the peaks to the functional groups (full spectra: Figure S3). For the calculation of the NIPAm/NEAm ratios, the peaks b and g are integrated and a NIPAm/NEAm ratio of ~1.5 is confirmed for all samples, proving that the chemical composition of all microgels is equivalent and corresponds to the quantity ratio initially used. The peaks arising below 2.2 ppm derive from the methyl groups (a + f) and from the backbone. For the backbone groups CH (d + i) and CH2 (e + k), different conformational structures due to intramolecular microgel interactions, as well as microgel-water interactions lead to numerous peaks with varying intensities.

In 3S and 4S microgels GT: 55 °C, physically entrapped water is detected at ~3.7 ppm and can be distinguished from free water or water interacting with the polymer network, which both appear at higher ppm values (~4.7–4.8).[22] Interestingly, the mobility of entrapped water does not significantly change at 60 °C as the NMR signal is still well pronounced. We attribute this effect to the formation of micropores that are not interconnected with each other so that water molecules cannot diffuse outwards during phase transition in contrast to microgels produced from MC and microgels crosslinked at room temperature.

As a next step, variable temperature NMR (VT NMR) is performed enabling quantitative characterization of the phase separated fraction ($p = 1-(I \times I_0^{-1})$) for individual functional groups at different temperatures. Here, I_0 is the NMR signal intensity at 25 °C and I the signal intensity at the respective temperature. The sum of all accessible methyl side groups on the polymer backbone (a + f) is analyzed as a function of the temperature (Figure 4b). The temperature dependent macromolecular phase transition is sharp for all star-based microgels, whereas a more gradual transition is observed for MC samples. This supports the results gained from bright field images (Figure 2a), where a sudden, clear morphology transition is only observed for star-based microgels. Since the 3S and 4S precursors remain dissolved during synthesis, a random distribution of both the monomers is expected even at GT: 55 °C, while for the monomer composition domains containing more PNIPAm will respond before the PNEAm starts collapsing. The experimental results show that for all star-based microgels and MC GT: 23 °C, the $p(T)$ course of b and g is equal, proving identical phase transition behavior for both monomer species (Figure 4a). For MC GT: 55 °C, however, a slightly different $p(T)$ course is observed for the NEAm and NIPAm groups (Figure S4), indicating the formation of block copolymer domains at GT: 55 °C, which is exceeding the LCST of PNIPAm but not PNEAm.

To demonstrate the shelf life of the microgels, we added images to the Supporting Information of microgels that were stored for three years in water at 4 °C (Figure S5). This shows that the microgels do not degrade for a long time and that there would be no degradation products affecting cell culture in follow-up experiments.

Conclusions

Achieving significantly different gel network morphologies from the same thermally assisted microfluidic setup by varying the described precursor systems allows for a significant diversification of the internal structures that impact the final microgel properties. Since gel characteristics like porosity, solvent diffusion, stiffness and thermo-responsivity are all highly dependent on network morphology and general composition of the polymer chains inside the network, the precursor characteristics are crucial for the resulting product. The MC precursor solution is affected in a significantly different way compared to the 3S and 4S macromolecule-based systems, which only undergo phase separation and precursor interaction change around the preset LCST of the multi-arm molecules, in contrast to the MC solution. Considering the obtained data, the choice of the precursor system in combination with thermally assisted microfluidics allows for fabrication of microgels with a wide

stiffness range from ~1.0 to 173.8 kPa, along with significant tuning of the morphology and thermoresponsive behavior, while maintaining the chemical composition of the gel network.

As cellular mechanotransduction and ECM formation of cells interacting with gels is affected by multiple parameters like local stiffness distribution, network architecture or porosity characteristics,[23] controlled diversification of chemically equivalent microgel network morphologies allows for more controlled mechanosensitive cell studies. The introduction of AuNRs into the microgels will allow for reversible volume actuation via an externally controlled NIR light source, as previously reported.[13c,17] This will provide a microgel-based photothermal volumetric system combining morphology variation and precise mechanical actuation.

Supporting Information

The authors have cited additional references within the Supporting Information.[24]

Acknowledgements

We gratefully acknowledge funding from the Deutsche Forschungsgemeinschaft (DFG) within the projects B5, C3 and C9 SFB 985 "Functional Microgels and Microgel Systems", the GRK2415 ME3T—Mechanobiology in Epithelial 3D Tissue Constructs, and the project LA 3606/2-2. We also acknowledge funding from the Leibniz Senate Competition Committee (SAW) under the Professorinnenprogramm (SAW-2017-PB62: BioMat) and the Werner Siemens Foundation (Project TriggerInk). Furthermore, we are grateful for funding from the European Commission (EUSMI, 731019). This work was performed in part at the Center for Chemical Polymer Technology (CPT), which was supported by the EU and the federal state of North Rhine-Westphalia (grant EFRE 30 00 883 02). .The work was mainly performed at the DWI - Leibniz Institute for Interactive Materials e.V. and the Institute for Technical and Macromolecular Chemistry at the RWTH Aachen University. Parts of the study have been published in the PhD thesis of Dirk Rommel. Open Access funding enabled and organized by Projekt DEAL.

Conflict of Interest

The authors declare no conflict of interest.

Data Availability Statement

The data that support the findings of this study are available from the corresponding author upon reasonable request.

Keywords: Internal Structure · Mechanical Properties · Microfluidics · Thermoresponsiveness · Morphology

[1] a) Q. Feng, D. Li, Q. Li, X. Cao, H. Dong, *Bioact. Mater.* **2022**, *9*, 105–119; b) Y. Kittel, A. J. C. Kuehne, L. De Laporte, *Adv. Healthcare Mater.* **2022**, *11*, 2101989.
[2] a) Y. Hu, Q. Wang, J. Wang, J. Zhu, H. Wang, Y. Yang, *Biomicrofluidics* **2012**, *6*, 026502; b) L. P. Guerzoni, J. C. Rose, D. B. Gehlen, A. Jans, T. Haraszti, M. Wessling, A. J. Kuehne, L. De Laporte, *Small (Weinheim an der Bergstrasse, Germany)* **2019**, *15*, 1900692.
[3] H. J. Wolff, J. Linkhorst, T. Göttlich, J. Savinsky, A. J. Krüger, L. De Laporte, M. Wessling, *Lab Chip* **2020**, *20*, 285–295.
[4] J. Guan, N. Ferrell, L. James Lee, D. J. Hansford, *Biomaterials* **2006**, *27*, 4034–4041.
[5] S. P. O. Danielsen, H. K. Beech, S. Wang, B. M. El-Zaatari, X. Wang, L. Sapir, T. Ouchi, Z. Wang, P. N. Johnson, Y. Hu, D. J. Lundberg, G. Stoychev, S. L. Craig, J. A. Johnson, J. A. Kalow, B. D. Olsen, M. Rubinstein, *Chem. Rev.* **2021**, *121*, 5042–5092.
[6] S. Seiffert, *Prog. Polym. Sci.* **2017**, *66*, 1–21.
[7] Y. Kittel, L. P. Guerzoni, C. Itzin, D. Rommel, M. Mork, C. Bastard, B. Häßel, A. Omidinia-Anarkoli, S. P. Centeno, T. Haraszti, *Angew. Chem. Int. Ed.* **2023**, *62*, e202309779.
[8] a) W. Richtering, B. R. Saunders, *Soft Matter* **2014**, *10*, 3695–3702; b) J. R. Höhner, R. A. Gumerov, I. I. Potemkin, C. Rodriguez-Emmenegger, N. Y. Kostina, A. Mourran, J. Englert, D. Schröter, L. Janke, M. Möller, *Macromolecules* **2022**.
[9] a) R. H. Pelton, P. Chibante, *Colloids Surf.* **1986**, *20*, 247–256; b) A. Pich, W. Richtering, in *Chemical Design of Responsive Microgels* (Eds.: A. Pich, W. Richtering), Springer Berlin Heidelberg, Berlin, Heidelberg, **2011**, pp. 1–37; c) O. L. J. Virtanen, M. Kather, J. Meyer-Kirschner, A. Melle, A. Radulescu, J. Viell, A. Mitsos, A. Pich, W. Richtering, *ACS Omega* **2019**, *4*, 3690–3699.
[10] a) B. Vijayakumar, M. Takatsuka, R. Kita, N. Shinyashiki, S. Yagihara, S. Rathinasabapathy, *Macromolecules* **2022**, *55*, 1218–1229; b) M. Karg, T. Hellweg, *Curr. Opin. Colloid Interface Sci.* **2009**, *14*, 438–450.
[11] J. E. Chung, M. Yokoyama, M. Yamato, T. Aoyagi, Y. Sakurai, T. Okano, *J. Controlled Release* **1999**, *62*, 115–127.
[12] W. Xue, M. B. Huglin, T. G. J. Jones, *Macromol. Chem. Phys.* **2003**, *204*, 1956–1965.
[13] a) Q. Wang, C. S. Biswas, M. Galluzzi, Y. Wu, B. Du, F. J. Stadler, *RSC Adv.* **2017**, *7*, 9381–9392; b) C. S. Biswas, Q. Wang, M. Galluzzi, Y. Wu, S. T. Navale, B. Du, F. J. Stadler, *Macromol. Chem. Phys.* **2017**, *218*, 1600554; c) Y. Chandorkar, A. Castro Nava, S. Schweizerhof, M. Van Dongen, T. Haraszti, J. Köhler, H. Zhang, R. Windoffer, A. Mourran, M. Möller, L. De Laporte, *Nat. Commun.* **2019**, *10*, 4027.
[14] S. Bharadwaj, B.-J. Niebuur, K. Nothdurft, W. Richtering, N. van der Vegt, C. M. Papadakis, *Soft Matter* **2022**.
[15] a) J. Kim, J. Yoon, R. C. Hayward, *Nat. Mater.* **2010**, *9*, 159–164; b) Z. Liu, Y. Liu, Y. Chang, H. R. Seyf, A. Henry, A. L. Mattheyses, K. Yehl, Y. Zhang, Z. Huang, K. Salaita, *Nat. Methods* **2016**, *13*, 143–146; c) V. Capella, R. E. Rivero, A. C. Liaudat, L. E. Ibarra, D. A. Roma, F. Alustiza, F. Mañas, C. A. Barbero, P. Bosch, C. R. Rivarola, N. Rodriguez, *Heliyon* **2019**, *5*, e01474; d) I. Sanzari, E. Buratti, R. Huang, C. G. Tusan, F. Dinelli, N. D. Evans, T. Prodromakis, M. Bertoldo, *Sci. Rep.* **2020**, *10*, 6126; e) A. Sutton, T. Shirman, J. V. Timonen, G. T. England, P. Kim, M. Kolle, T. Ferrante, L. D. Zarzar, E. Strong, J. Aizenberg, *Nat. Commun.* **2017**, *8*, 1–13.
[16] a) A. Nishiguchi, H. Zhang, S. Schweizerhof, M. F. Schulte, A. Mourran, M. Möller, *ACS Appl. Mater. Interfaces* **2020**, *12*, 12176–12185; b) A. Mourran, O. Jung, R. Vinokur, M. Möller, *Eur. Phys. J. E* **2021**, *44*, 79.

[17] a) Y. Chandorkar, C. Bastard, J. Di Russo, T. Haraszti, L. De Laporte, *Appl. Mater. Today* **2022**, *27*, 101492; b) A. Castro Nava, I. C. Doolaar, N. Labude, H. Malyaran, S. Babu, Y. Chandorkar, J. Di Russo, S. Neuss, L. De Laporte, *ACS Appl. Mater. Interfaces* **2024**, *16*, 30–43.
[18] a) A. Omidinia-Anarkoli, R. Rimal, Y. Chandorkar, D. B. Gehlen, J. C. Rose, K. Rahimi, T. Haraszti, L. De Laporte, *ACS Appl. Mater. Interfaces* **2019**, *11*, 7671–7685; b) C. Wu, M. Chen, T. Zheng, X. Yang, *Bio-Med. Mater. Eng.* **2015**, *26*, S155–S164; c) A. Riveiro, A. L. Maçon, J. del Val, R. Comesaña, J. Pou, *Front. Phys.* **2018**, *6*, 16.
[19] Y. Gao, D. Zhou, J. Lyu, S. A. Q. Xu, B. Newland, K. Matyjaszewski, H. Tai, W. Wang, *Nat. Chem. Rev.* **2020**, *4*, 194–212.
[20] a) G. Scarcelli, W. J. Polacheck, H. T. Nia, K. Patel, A. J. Grodzinsky, R. D. Kamm, S. H. Yun, *Nat. Methods* **2015**, *12*, 1132–1134; b) R. Schlüßler, S. Möllmert, S. Abuhattum, G. Cojoc, P. Müller, K. Kim, C. Möckel, C. Zimmermann, J. Czarske, J. Guck, *Biophys. J.* **2018**, *115*, 911–923.
[21] a) P. Van Der Scheer, T. Van De Laar, J. Van Der Gucht, D. Vlassopoulos, J. Sprakel, *ACS Nano* **2017**, *11*, 6755–6763; b) I. Bouhid de Aguiar, T. Van de Laar, M. Meireles, A. Bouchoux, J. Sprakel, K. Schroën, *Sci. Rep.* **2017**, *7*, 10223.
[22] T. M. Alam, K. K. Childress, K. Pastoor, C. V. Rice, *J. Polym. Sci. Part B* **2014**, *52*, 1521–1527.
[23] A. Jagiello, U. Castillo, E. Botvinick, *Sci. Rep.* **2022**, *12*, 11736.
[24] a) A. M. Bivigou-Koumba, J. Kristen, A. Laschewsky, P. Müller-Buschbaum, C. M. Papadakis, *Macromol. Chem. Phys.* **2009**, *210*, 565–578; b) S. Schweizerhof, D. E. Demco, A. Mourran, H. Keul, R. Fechete, M. Möller, *Macromol. Chem. Phys.* **2017**, *218*, 1600495; c) Y. Qu, X. Chang, S. Chen, W. Zhang, *Polym. Chem.* **2017**, *8*, 3485–3496; d) A. J. D. Krüger, O. Bakirman, L. P. B. Guerzoni, A. Jans, D. B. Gehlen, D. Rommel, T. Haraszti, A. J. C. Kuehne, L. De Laporte, *Adv. Mater. (Deerfield Beach, Fla.)* **2019**, *31*, e1903668; e) D. Rommel, M. Mork, S. Vedaraman, C. Bastard, L. P. B. Guerzoni, Y. Kittel, R. Vinokur, N. Born, T. Haraszti, L. De Laporte, *Adv. Sci. (Weinh.)* **2022**, *9*, e2103554; f) T. L. Bergman, T. L. Bergman, F. P. Incropera, D. P. Dewitt, A. S. Lavine, *Fundamentals of heat and mass transfer*, John Wiley & Sons, **2011**; g) H. Hertz, *J. fur Reine Angew. Math.* **1881**, *92*; h) K. Kim, J. Guck, *Biophys. J.* **2020**, *119*, 1946–1957; i) E. Cuche, P. Marquet, C. Depeursinge, *Appl. Opt.* **2000**, *39*, 4070–4075; j) E. Wolf, *Opt. Commun.* **1969**, *1*, 153–156; k) Y. Sung, W. Choi, C. Fang-Yen, K. Badizadegan, R. R. Dasari, M. S. Feld, *Opt. Express* **2009**, *17*, 266–277; l) K. Kim, H. Yoon, M. Diez-Silva, M. Dao, R. R. Dasari, Y. Park, *J. Biomed. Opt.* **2014**, *19*, 011005–011005; m) S. Zhou, S. Fan, S. C. Au-yeung, C. Wu, *Polymer* **1995**, *36*, 1341–1346; n) R. Barer, *Nature* **1952**, *169*, 366–367; o) R. Schlüßler, K. Kim, M. Nötzel, A. Taubenberger, S. Abuhattum, T. Beck, P. Müller, S. Maharana, G. Cojoc, S. Girardo, *eLife* **2022**, *11*, e68490; p) A. Thakare, *Int. J. Eng. Res.* **2015**, *04*, 92–99.

Manuscript received: June 23, 2024
Accepted manuscript online: October 25, 2024
Version of record online: November 14, 2024